A joint methodical case study for understanding severe formation clogging processes within a highly utilized geothermal reservoir in the Pannonian Basin of Hungary

Rita Mwendia Njeru[1], *Matthias* Halisch[2 *], *Arne* Jacob[3], *Andreas* Weber[3], *Péter* Koroncz[4,5], *Ferenc* Fedor[4,5], *János* Szanyi[1]

[1]University of Szeged, Department of Mineralogy, Geochemistry and Petrology, Egyetem street 2, 6722 Szeged, Hungary
[2]LIAG Institute for Applied Geophysics, Stilleweg 2, D-30655 Hannover, Germany
[3]Math2Market GmbH, Richard-Wagner-Straße 1, D-67655 Kaiserslautern, Germany
[4]Geochem Geological and Environmental Research, Consultancy and Service Ltd., 7673 Kővágószőlős, Hungary
[5]Institute of Geography and Earth Sciences, University of Pécs, 7624 Pécs, Hungary

Abstract. Geothermal energy is a promising renewable energy source, considering the costs of fossil energy and the need to reduce greenhouse gases drastically. The Dunántúli Group (DG, a sandstone formation), located in the Hungarian part of the Pannonian Basin, stands out as being most promising for Hungary´s national geothermal energy production. Currently, over 600 operational wells targeting the DG exist in Hungary. Although a 1:2 ratio of production to reinjection wells is targeted for this reservoir, only 5% of all wells serve reinjection purposes. Limited knowledge exists about microscale pore structures and flow properties of this formation, crucial for both, successful water reinjection and for geothermal energy extraction. Severe clogging processes afflict geothermal wells in this region, shutting down injection wells within a very short amount of time, causing significant extra costs and delays in progressing Hungary´s energy transition. This study investigated selected reservoir samples from the DG, utilizing classical mineralogical and petrophysical methods, an extensive core-flooding program for controlled clogging of artificial and natural core samples, as well as X-ray µ-CT imaging, qualitative and quantitative 3-D image analysis and pore scale simulations with special focus upon the physical pore clogging. Due to the influence of (micro-) tectonic activities, many micro-fractured and hence potentially movable grains can be found (e.g., movable by re-injection of formation water). Although the storage properties are favourable, pore throats, which control fluid flow, are nearly of the same size as the movable particles within the pore-system. This fact, coupled with smaller particles present in the re-injection fluid, leads to significant and deep-seated clogging of flow pathways. Furthermore, the absence of cement in the permeable part of the DG will cause formation compaction during reinjection, if pressures are higher compared to the formation pressure. This leads to a reduction of the average pore throat size, causing progressive clogging of the entire injection zone. For the first time, these processes have been validated successfully through pore-scale clogging simulations using GeoDict software. These results significantly enhance the understanding of transport in the DG as they provide insights into the geology and hydrogeology of the Pannonian Basin, encouraging industry and scientists to develop and drill more and sustainable reinjection wells.

1 Introduction

Geothermal energy utilizes the Earth's internal heat to generate electricity and provide heating, offering a sustainable baseload alternative to fossil fuels., It is accessed through wells drilled into geothermal reservoirs and transported by fluid; water or steam. To maintain these reservoirs' efficiency and longevity, reinjection of spent geothermal fluids is essential. The injection of energy depleted thermal fluid is necessary for two main reasons: to compensate for the loss of pressure in the aquifer and to avoid contamination of surface receptors. Most important, it is crucial for continuous energy extraction. In the Pannonian Basin, the most extensively exploited geothermal reservoir is the Late Miocene's Dunántúl Group (DG), which comprises the alluvial plain sediments (Zagyva Formations) and delta plain sediments (Újfalu Formation).

With a geothermal gradient in between 45–50 °C per 1000m depth, the area around the cities of Szentes and Szeged are favorable spots for producing geothermal

* Corresponding author: matthias.halisch@leibniz-liag.de

energy [1, 2]. There have been successful and less successful geothermal projects with special regards to reinjection of produced geothermal fluids. The latter being the case of Mezőberény [3, 4, 5]. Currently, efficient reinjection in sandstone reservoirs in the Pannonian Basin is practiced on a limited scale due to limited design/demonstration experience in the area [6]. There are 84 injection wells in Hungary, 62 in porous reservoirs [7], but only half of them are in operation due to insufficient regulation to allow this [8]. There are currently about 300 wells producing energy without injection from DG [4], and with the latest geothermal strategy, the country wants to double the amount of geothermal energy it produces by 2030. In addition, there are numerous other wells in neighbouring countries within the Pannonian Basin, which are situated in the same reservoir. This makes the systematic study of microscale reinjection processes in DG sandstones even more important.

The need for reinjection predates the exploitation of geothermal reservoirs. However, injectivity can be significantly affected by various clogging processes that result in pore blockage and a reduction in permeability [9]. In unconsolidated media, an additional problem is the shear forces between the flowing fluid and the porous media, resulting in moving particles [10]. For almost 50 years, the oil industry has been injecting water back into the sandstone formations of the DG at very high pressures, sometimes in excess of 100 bar, to extract secondary hydrocarbons. This technology is highly uneconomical and unsustainable in the long term for thermal water [3]. The loss of injectivity in geothermal reservoirs, particularly within the Pannonian Basin's sandstone formations, is often accelerated by physical clogging mechanisms.

This reduction in permeability poses significant challenges for sustainable geothermal energy production. Despite widespread recognition of these challenges, current strategies to mitigate clogging are largely inadequate, often failing to address the microscale interactions that are crucial for understanding and preventing clogging phenomena effectively. Therefore, our research aims to fill this gap by focusing on the microscale processes that contribute to clogging during reinjection, which has been less explored in existing studies. We use a combination of laboratory-scale simulations and microscale analytical techniques to address the critical aspects of physical clogging. By applying these methods, we aim to contribute towards developing a more effective approach to maintaining injectivity and enhancing the operational longevity of geothermal wells.

2 Geological Background

The Pannonian Basin, located in in Central and Eastern Europe is divided into eight countries, with Hungary occupying the central part (Figure 1A). It evolved during the Neogene as an integral part of the Alpine, Carpathian, and Dinaric mountain building system. During the Miocene, as the mountains uplifted, the Pannonian basin subsided. In the Pannonian Lake, which occupies the area, more than 7000m m of mostly clastic sediment has been deposited due to intense erosion of the mountains [11, 12, 13]. The basement is covered by early Miocene sediments, after which mainly deep-sea marls and turbidites were deposited; this low permeability sequence is called the Alföld Group. After that, deltaic sediments such as sandstone, siltstone and clay were deposited. These are called the Újfalu Formation, followed by alluvial plain sediments of sand, silt and clay, called the Zagyma Formation. The latter two formations are known together as the DG [14, 15, 16] (Figure 1B).

The thickness of the Újfalu Formation exceeds 1000m, with one-third comprising sandstone. The permeability of these rocks varies considerably, spanning from low (couple of mD) to 2 Darcy and its porosity can reach 30%. [8, 17]. This wide range is attributed to the heterogeneous nature of the formation and varying degrees of consolidation and mineral composition across different sections of the formation. Together with the overlying Quaternary sediments, the DG forms a uniform gravity flow system, its pressure being hydrostatic [15]. The Újfalu Formation is used for most of the thermal water production in the Great Hungarian Plain, an extensive flat region in Hungary known for its significant agricultural and aquifer systems.

The thermal wells in the most intensively produced region of Szentes, where about 40 thermal wells are in operation, supplying water with a temperature of 60 – 102°C. As a result of operating without a single reinjection well, the average static water level of 30-50 m was observed [8]. It is for this reason that we decided to analyse a newly drilled well in the area (Figure 1C).

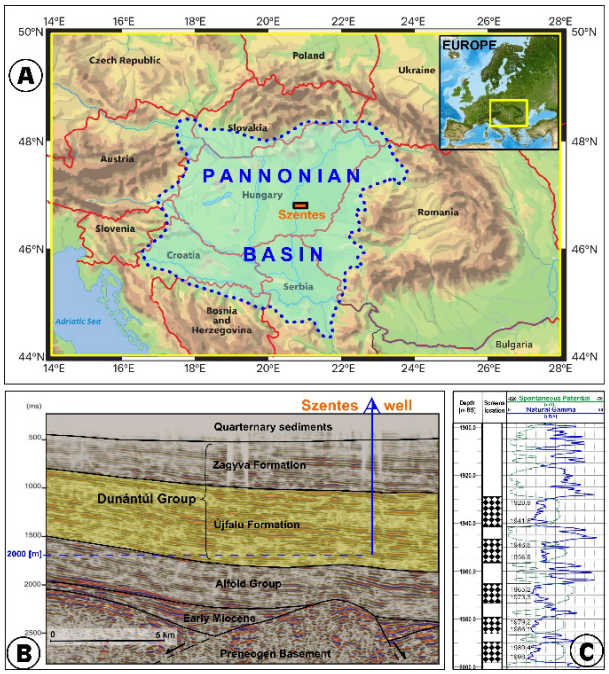

Fig. 1. A) Location of the Pannonian Basin with study site, based on [18]; B) Interpreted seismic section in the region of Szentes showing the location of the well being investigated, based on [19]; C) Geophysical log of the studied well, based on [20].

3 Sample Material

For systematic studies of clogging processes, always a sufficient amount of core material is needed. But without the neccessity to reinject thermal fluids by law, and by also knowing the DG formation is a very productive reservoir, literally no cores are taken during drilling, to avoid these extra costs. And as a matter of fact, thermal fluids are dumped on the surface in many cases. For this study, core plugs from the only publically available drilled core have been prepared for a basic analysis. Nevertheless, due to the limited amount of material, artificial core plugs have been specially designed to act as proxies for future systematic core analysis and studies in the laboratory.

3.1 Natural Core Samples

For our study, representative sandstone core samples extracted from a depth between 1936 m and 1960 m in the DG were studied. The core samples were cut from 8 m of the drill core to obtain samples of 37 mm in diameter and height. Three representative samples have been used for our study, covering the main features and structures of the DG important for a successful reinjection of fluids. Sample preparation was carried out at the GeoChem Limited laboratories, Hungary (https://geochem-ltd.eu//). The representative samples feature coarse, medium, and fine sand grains, respectively. They exhibit varying degrees of cementation, scaling with their porosity (lower porosity equals higher cementation, higher porosity equals lower cementation). X-ray diffraction analysis revealed that the main component for all samples is quartz, followed by feldspars, mica, and non-swelling clay minerals (according to XRD-results: 45-60 w.-% SiO2; 20 w.-% feldspars, mostly plagioclase; 7 w.-% muscovite; 10 w.-% chlorite; 3 w.-% kaloninite; 9-20 w.-% CaCO3; 1 w.-% residuals).

The petrophysical measurements have been challenging to perform, due to the unconsolidated nature of the rock samples. Nevertheless, it was possible to derive reproducible and hence reliable data for a general characterization. The effective porosity is high, ranging from approx. 27% - 31 %, and are in good accordance with the degree of cementation that has been visually detected. Gas-permeability follows this trend, ranging from about 60 mD for the 27% porosity sample, to 400 mD for the 31% porosity sample. Remarkably, a significant permeability increase (factor of 4) was observed in between porosity ranges from 28 – 29%. This might indicate a crucial pore throat size change, dominating the flow properties and hence most likely physical clogging processes as well. Figure 2 (top) shows a representative 2D µ-CT image and the according natural sample.

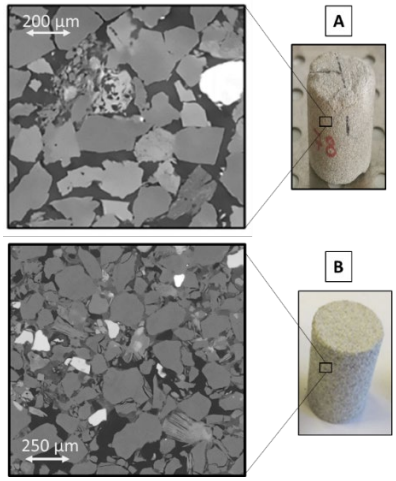

Fig. 2. Representative 2D µ-CT image and according core plug of the natural (A) and artificial (B) core samples used for this study.

3.2 Artificial Core Samples

Artificial core samples were prepared by using drill cuttings from the DG formation, natural sand, and carbonatic binder material. The selection of natural sand was necessary because grains from the DG formation cracked during the preparation process. Hence, the natural sand worked as replacement, featuring similar shapes and sizes. The wet mixture of fluvial sand from the

Drávaszabolcs area in Hungary (close to the Croatian boarder) and analytical reagent quality $Ca(OH)_2$ was poured into a stainless-steel cell and compacted with a hydraulic press. After compaction, the samples were stored in a pressurized chamber filled with CO_2 gas. This step helps the formation of carbonate cement minerals. Figure 2 (bottom) shows a representative 2D µ-CT image and the according artificial sample. Table 1 summarizes the main petrophysical features of these rocks related to the natural sample thes have been designed from.

Table 1. Average porosity and permeability values of the natural and artificial core samples

sample / batch ID	state	porosity (%)	permeability (mD)
MMDR_131_1M_T	artificial	30	318
MMDR_131_2M_T	artificial	30	373
MMDR_132_2M_T	artificial	30	364
SZSZT_IX_31_T	natural	28	320

4 Setup to Assess Clogging

The schematic diagram of the experimental setup is illustrated in Figure 3. This setup was designed to simulate in-situ conditions of geothermal reservoirs, enabling detailed analysis of clogging mechanisms.

Plug samples were placed into a triaxial core holder (Fig.3, CE-01), where the confining pressure was adjusted by a plunger pump to a precise setting of 15 bar, within a tolerance of +/- 0.5 bar. This configuration mimics the stress conditions encountered within actual geothermal reservoirs, providing a realistic basis for our experiments.

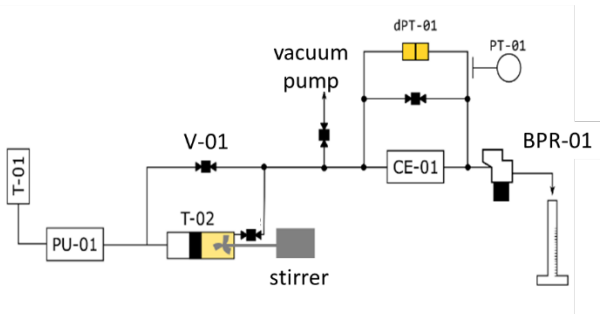

Fig. 3. Schematic of experimental setup for core flooding tests.

For water permeability measurements, brine water composed of 2% potassium chloride (KCl) was pumped from a fluid container (Fig.3, T-01) using a high-precision HPLC pump (Fig.3, PU-01). This pump ensures a pulsation-free constant flow rate, adjustable from 0.02 to 10 ml/min in 0.01 ml/min increments. Initially, the flow rate was set to 0.5 ml/min, incrementally increasing to a maximum of 4 ml/min. This brine had been previously vacuumed to eliminate any gas bubbles, which could potentially cause clogging effects themselves.

The initial clogging experiments involved using two types of barium sulphate ($BaSO_4$) particles: commercial particles with a diameter of 2 µm and drilling fluid particles with a size of approximately 20 µm. These experiments posed significant challenges. The high-density $BaSO_4$ particles caused premature clogging within the injection apparatus, hindering the delivery of particles into the sample cores. This occurred primarily because the particles settled in the pipes, preventing effective pumping through the samples. To tackle this problem, we modified the experimental setup. By employing hydraulic pressure for fluid injection and implementing continuous stirring to keep the particles suspended. Additionally, we transitioned to using less dense clogging particles to alleviate settling issues and ensure consistent delivery into the core samples, thus enabling a more accurate simulation of the clogging processes.

Finally, a suspension comprising 0.2% calcium metasilicate ($CaSiO_3$) of particle size 10 – 17 µm in 2% KCl was prepared and placed into an accumulator unit (Fig.3, T-02) equipped with a built-in stirrer. This setup maintained the suspension in a stirred state, ensuring consistent particle distribution and preventing settling. The suspension was injected into the system at a constant rate of 4 ml/min, facilitated by valves V-01 and V-02, allowing for fluid switching under continuous flow without disrupting the system's pressure equilibrium.

Pressure drops across the investigated plug samples were automatically recorded every 10 seconds using a differential pressure transducer (Fig.3, DPR-01) with a resolution of 0.001 bar. Absolute pressure was similarly monitored on the output side with a PT-01 transducer featuring a 0.1 bar resolution. These measurements were integral to tracking the progression and intensity of clogging as the experiments progressed.

Data on pressure and temperature parameters were continuously collected and stored alongside the time of recording, allowing for detailed monitoring and analysis. This comprehensive data collection was crucial for evaluating the experimental conditions as pressure settings, fluid compositions, and particle concentrations, as well as their impact on clogging within the operational timeframe. The methodology ensured a degree of clogging within the operational time while still accurately mimicking the geothermal reservoir conditions, thereby effectively studying the clogging phenomena.

All tests were conducted at room temperature, with continuous registration of temperature data to ensure consistency throughout the experimental process. After testing, cores were carefully removed, weighed, and dried at a controlled temperature of about 65°C, critical for maintaining sample integrity and facilitating accurate post-experiment analysis.

The experiments were repeated using new artificial samples. Finally, a control test was carried out by flooding an artificial sample using only the 2% KCl for a period equal to clogging experiments. Using artificial samples as identical as possible (validated by basic petrophysical analysis) was essential for assessing intra-test consistency, given the inherent heterogeneity of natural samples. This approach minimized variability in the results, enabling us to attribute observed differences directly to the experimental conditions rather than sample discrepancies. Also, a final test was carried out using a natural sample that was as similar as possible to the artificial sample and that is a target reservoir for geothermal reinjection but naturally suffers from clogging processes. Using the differential pressure data, we calculated the dimensionless impedance function $J(t_D)$ according to equation (1):

$$J(t_D) = \frac{\Delta P(t_D)\, q_0}{q(t_D)\, \Delta P(0)} = \frac{k_0}{k(t_D)} \qquad (1)$$

where $\Delta P(t_D)$ is the pressure difference at time (t_D) and q_0 is the constant flow rate. This approach, adapted from [21], provided a structured way to quantify permeability changes due to clogging in addition to enabling us to compare the injection results for different samples. For the clogging experiments, we aimed to identify one or more of the three specific clogging phenomena as defined by [3]: Surface filtration, deep filtration, or no filtration.

5 Pore Scale Simulations

The pore scale simulations have been performed with the GeoDict digital material laboratory software, developed and distributed by Math2Market [22]. 3D micro-CT images, derived at a voxel resolution of 1.5 µm have been processed as described by [23] and cropped to digital volumes with approximately 1000-1500 voxels (i.e., 1.5 mm to 2.5 mm length). For simulating digital core clogging, the following steps have been performed on each geometry.

5.1 Filtration Calculation

GeoDict uses a pseudo steady-state approach to calculate filtration on the micro-scale. Flow and particle movement are calculated in batches. We assume steady-state flow and unchanged structure geometry during this batch. At the beginning of each batch, the flow is solved for the current structure geometry. This flow field is then used to inject and transport particles through the structure. At the end of a batch, deposited particles are converted into part of the solid structure geometry. Repeating this process results in a buildup of deposited particles in the structure, usually an increase in pressure drop, a decrease in permeability and finally complete clogging of the structure's pore space.

5.2 Flow Calculation

The Navier-Stokes-Brinkman equations (2) are used in the filtration simulations to compute the fluid flow [24, 25]. Due to the creeping flow through the pores, the equations are usually simplified to the Stokes equations by dropping the nonlinear (inertia) term (remark: our assumption for being in creeping flow regime holds, as we are on average well below the Reynolds numbers that indicate turbulent flow for this characteristic length-scale. In porous media, a critical Reynolds number typically lies around 10 to 100. In this case, the Reynolds number is 6.32035e-10 for a characteristic length of 4.82786e-07 m in sample MMDR131_1M_S1). We also neglect the Brinkman term in this work, since we do only track particles with a size larger than a voxel. If a particle deposits within a pore, the corresponding voxels are blocked for any further flow and considered as 'solid' material. No porous, i.e., partially filled voxels are considered for solving flow or particle collisions.

$$\mu \Delta u - \rho(u \cdot \nabla)\, u - \mu \kappa^{-1} u = \nabla p \text{ on } \Omega, \qquad (2)$$

$$\text{with } \nabla \cdot u = 0 \text{ on } \Omega,$$

$$\text{and } u = 0 \text{ on } \Gamma,$$

where Ω = numerical domain, u = velocity, p = pressure, μ = dynamic viscosity, Γ = solid surface, ρ = density, κ = porous voxel permeability.

5.3 Particle Movement

The particle motion is modeled by a Lagrangian approach. Equation (3) gives the precise formulation for the particle transport without collisions in the most general form. As the particles are tracked with the fluid, two terms contribute to the particle velocity. The radius and density (as mass) enter the friction of the particle against the flow, and also into the diffusive part of the motion.

$$m\frac{d\vec{v}}{dt} = 6\pi\mu\frac{R}{C_c}\left(\vec{u} - \vec{v} + \sqrt{2D}\frac{d\vec{W}(t)}{dt}\right) + \mathrm{Q}\vec{\mathrm{E}} \qquad (3)$$

where $\vec{v}$ = particle velocity [m/s], $\vec{u}$ = fluid velocity [m/s], R = particle radius [m], Cc = Cunningham correction, m = particle mass [kg], μ = dynamic viscosity [kg/ms], Q = particle charge [C], E = electric field [V/m], D = diffusivity [m²/s] and $d\vec{W}$ = 3D Wiener process.

Particles can be positioned anywhere in pore space, while the fluid velocity is only available at a discrete set of points in space, for example on cell walls in case of one particular finite difference solver. To approximate fluid velocities at all particle locations, these discrete velocity values are linearly interpolated, while also considering no-slip boundary condition on any surface. The particles will not be able to interact with each other while in fluid flow. Thus, each particle can be simulated independently, which enables easy parallelization of the simulation code.

5.4 Particle Deposition

The flow and collision models account for mechanism of filtration. Except for the influence of their mass and electrical charges, particles follow the streamlines and can be caught by direct interception. Due to their mass, they can leave streamlines and can be caught by inertial impact. For small particles, the effect of Brownian motion is significant, and they can be caught by diffusive deposition. Naturally, large particles will be spatially hindered to move on by small pore throats.

Deposited particles are converted from the Lagrangian space into solid voxels, blocking flow and later particles coming their way. Each deposited particle may overlap with voxels only partially, adding to the overall solid volume fraction in these voxels. A solid voxel is only considered if at least 50% of its volume is overlapped by particles. Considering that in each batch, there are several particles deposited in the structure, it can happen that multiple particles deposit on the same voxels, since particles do not interact while moving. The overlap between two particles is considered a volume error, which should be minimized. Especially for the case shown here, where only few narrow paths through the structure exist, particles will accumulate at similar positions and volume error is generally high. To circumvent this issue, the number of injected particles must be reduced, which also reduces probability of particles depositing at the same position.

6 Results

6.1 Laboratory Clogging

Artificial samples: $J(t_D)$ is a dimensionless function that is plotted against a dimensionless time, to be able to compare and interpret results of different flow experiments (compare equation (1)). The $J(t_D)$ curve of our experiments (Figure 4) shows an initial decrease in permeability, suggesting that clogging begins soon after the injection process starts. This could be due to immediate blockage from the particle-laden fluid. A stable phase is later observed, which may indicate a temporary balance between injection and clogging. However, the artificial samples show an increase in permeability after the initial clogging, as indicated by a decrease in $J(t_D)$. This is counterintuitive to clogging expectations and suggests a reorganization within the pore structure. This could be the result of reorientation of grains within the artificial core. Other possible cause of the permeability increase could be dissolution of the sample's cement material.

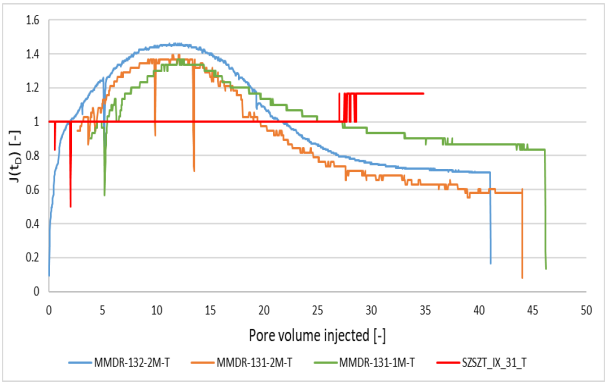

Fig. 4. Dimensionless flowrate versus injected pore volumes of the clogging experiments.

There is no evidence of subsequent clogging in the artificial samples. The control experiment reinforces this observation, as it shows that although no or very locally distributed filter cake (Figure 5, A) is formed the same distribution is observed as in the experiments that showed physical evidence of filter cake. This suggests that the clogging observed initially may not be a deep filtration but a rearrangement of the sample grains, cement dissolution or opening of new flow channels within the artificial core. Due to XRD analysis, we can neglect swelling clays causing this behavior.

Natural samples: For the natural samples, the $J(t_D)$ data shows a stepwise decrease in permeability without recovery, indicating a gradual and continuous process of clogging. This behavior is likely due to the inherent heterogeneity and complexity of the natural rock's pore network, where different pathways are sequentially closed. The absence of recovery in the natural samples' permeability implies that the clogging is effectively irreversible under the conditions tested. This matches the conclusion that clogging in natural samples is a significant

and persistent problem that leads to a decrease in injectivity. For all samples, a filter cake was observed (Figure 5, B), but the implications for the formation are different for each. In artificial samples, the lack of long-term clogging despite filter cake formation suggests that the cake does not lead to sustained reductions in permeability. In contrast, the natural samples exhibit ongoing clogging, which might be further accelerated by filter cake formation.

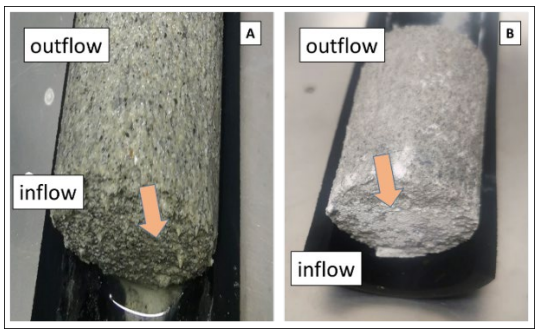

Fig. 5. Different types of filter cake evolution observed for the samples: left (A) = locally, right (B) = inflow covering.

6.2 Image Based Assessment of Clogging

The samples have been investigated by 3D µ-CT after the clogging experiments. The samples have been scanned at the full field of view, achieving a true voxel resolution of 15 µm, capturing 80% of the sample´s entire length (i.e., getting the entire inflow and flow region). The resulting 3D data sets have only been basically processed (filtered, cropped in x- and y-dimension to avoid artifacts), and have been evaluated for their porosity profiles alongside the z-axis (in direction of flow).

Please note: all different samples have been micro-CT scanned in the same region of interest with the same resolution, before and after the clogging experiments, to be sure that any changes could be clearly related to the blockage of pores. Additionally, for each of the samples (clogged and unclogged) sub-volumes close to the inflow, middle, and outflow regions have been prepared and scanned at 3 µm voxel resolution for better assessment of spatial variations and / or differences. For case of this paper, we will only highlight the overview scans (@ 15 µm) and one inflow region sub-sample scan (@3 µm).

Artificial samples: Figure 6 highlights the porosity distribution alongside the z-axis (flow direction from bottom to top) for one of the clogged artificial samples. The porosity was derived slice by slice in z-axis and after segmenting grains and pore space. For better alignment of the data, the air volume at the inflow has not been cropped from the image data. Because of this, resulting volume fraction curves for grains and pores (Figure 6, right hand side) overlap, followed by a small transition zone caused by the surface roughness of the sample top. From about 0.5mm onwards, a distinct increase in porosity (about 50%) from inflow (Figure 6, bottom) towards the outflow region (Figure 6, top) was observed. After 2.5 cm, porosity values start to flatten out, i.e., tend to reach constant values. In this case, a deep infiltration of roughly 2/3 of the sample´s length has been achieved.

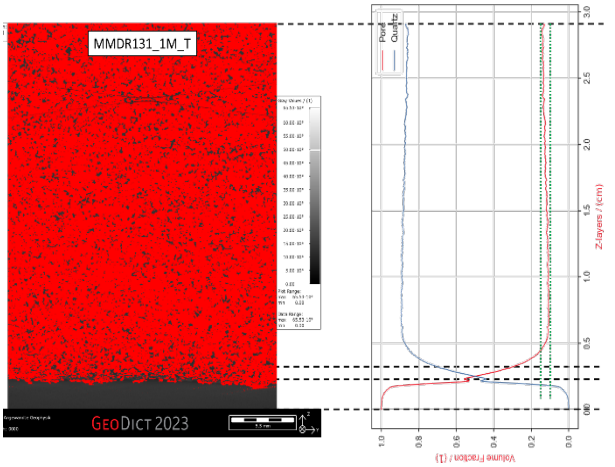

Fig. 6. Porosity profile for the artificial sample in direction of flow (from bottom to top of the sample). The left hand side shows the segmented rock (red = grains, black = pore space). On the right hand side the volume fraction distribution for both phases are shown (grains = blue line, pores = red line). A distinct increase in porosity from inflow in direction of outflow is noticeable.

Natural samples: Figure 7 highlights the porosity distribution alongside the z-axis (flow direction from bottom to top) for one of the clogged natural samples. The porosity was derived slice by slice in z-axis and after segmenting grains and pore space. As before, for better alignment of the data, the air volume at the inflow has not been cropped from the image data. Because of this, resulting volume fraction curves for grains and pores (Figure 7, right hand side) overlap, followed by a small transition zone caused by the surface roughness of the sample top. From about 0.6 mm to 10 mm at the inflow region, a small porosity increase is visible. Nonetheless, the porosity profile from that point on remains remarkably constant, only showing some local heterogeneity caused by a lesser cemented region close to the outflow zone. Conclusively, the infiltration was much shallower (i.e., less than half way in comparison) for the natural sample as for the artificial one.

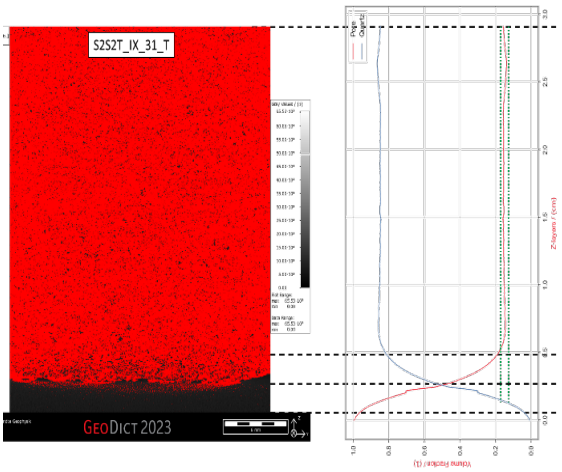

Fig. 7. Porosity profile for the natural sample in direction of flow (from bottom to top of the sample). The left hand side shows the segmented rock (red = grains, black = pore space). On the right hand side the volume fraction distribution for both phases are shown (grains = blue line, pores = red line). Though an increase in porosity within the first 5-8mm of the sample is noticeable, it is not as pronounced as for the artificial rock.

Assessing the higher resolution sub-volume µ-CT scan for this specimen (Figure 8), the porosity increase becomes distinctly. Nevertheless, the total increase is in range of 10-15% of the maximum observed porosity for this dataset. After 3.5 mm to 4 mm in, the porosity profile already starts to flatten out. A comparison with a sub-sample from deeper inside of the main flow region confirmed this finding of a shallow infiltration. At this point, the assumptions and data of the laboratory experiments have been confirmed.

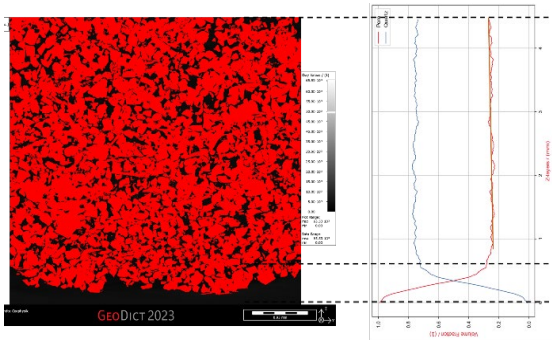

Fig. 8. Porosity profile of the inflow region for the natural sample in direction of flow (from bottom to top of the sample). The left hand side shows the segmented rock (red = grains, black = pore space). On the right hand side the volume fraction distribution for both phases are shown (grains = blue line, pores = red line). The porosity change is now more clearly visible due to the higher image resolution of 3µm.

6.3 DRP and Simulated Clogging

The observed changes in porosity are conclusive about the laboratory experiments. Nevertheless, for understanding these different types of infiltration behavior, digital rock physics (DRP) simulations are capable of adding substantial knowledge. Each of the samples, i.e., natural and artificial, have been scanned by µ-CT in "clean state" (i.e., before clogging) with 1.5 µm voxel resolution. These datasets have been utilized for systematic digital experiments, including:

- clogging simulations (as described in chapter 5),
- capillary pressure (MICP) simulations [26-35],
- fluid flow simulations [24, 25].

The latter two DRP simulations have been performed before and after the digital clogging. The particle size distribution for the clogging simulation was close to the one used for the laboratory experiments.

Since fluid flow, and hence the infiltration of particles into the samples, is dominated by the narrowest pore within the widest flow path, i.e,. by the pore throats of the pore networks, results from digital MICP simulations, combined with results from the permeability development during the clogging simulation are shown first. Spatial particle agglomerations as well as infiltration depths for the DRP datasets are highlighted afterwards. Please note that due to the higher image resolution, resulting numerical domains are much smaller than the coarser scans performed for the general assessment of the laboratory experiments, which explains the "spiky" distribution in the simulated MICP in Figure 9. Nevertheless, knowing that absolute numbers might not be representative, we were mainly interested in where and why the clogging happens, and if we generally can reproduce the macroscopic observations regarding infiltration depth.

Artificial sample: Figure 9 displays the results of the MICP simulations before (Figure 9, blue line) and after (Figure 9, red line) the digital clogging. The dashed red line indicates changes in between. Two main observations can be drawn, if the very similar looking data curves are compared more in detail. First, the most significant reduction of pore throat diameters (PTD) occurred around 20 µm, and in between 35 – 50 µm. This reduction can be related to the clogging of flow paths within the domain. Second, an increase in volume fraction of pore throats around 5 – 7.5 µm, which is most likely related to inter-granular throats that have formed in between the clogged, i.e., agglomerated and infiltrated particles. The remaining throats in between these areas are remarkably constant and undisturbed.

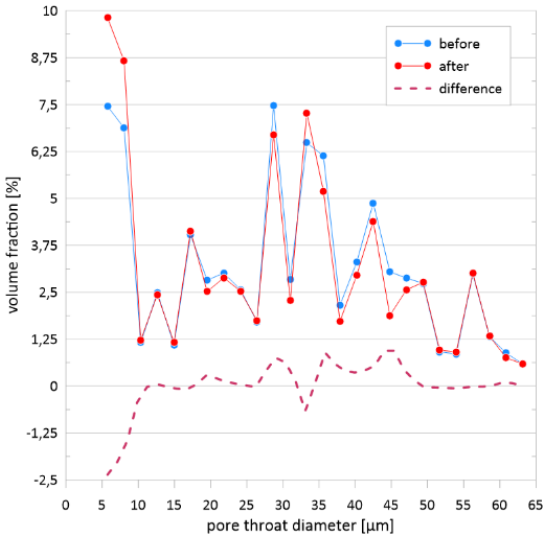

Fig. 9. Results of the MICP simulations for the artificial sample, before (blue line) and after (red line) digital clogging. The dashed red line displays the difference of both curves.

Figure 10 displays the according distribution of permeability and porosity over time for the clogging simulation. The overall change in porosity is not very remarkable, but at least constantly decreases during the simulation. The numerical domain obviously was too small to achieve a representative volume for the targeted parameters. Nevertheless, the permeability decrease over time is very pronounced and happens in two time steps. The first significant decrease happens within the first two hours of the simulation. A second, less pronounced decrease happens after 10 hours of digital injection. Our assumption is that two main flow paths, or flow paths with two different ranges of pore throat sizes, have been stepwise clogged, leading to this result.

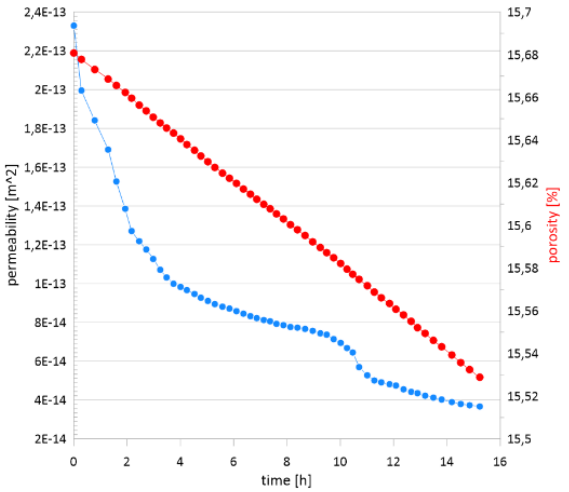

Fig. 10. Development of permeability for the artificial sample during the digital clogging simulation (blue line). The red line displays the porosity change over time.

In fact, a close look into the digital sample before and after the clogging simulation revealed very locally distributed, i.e., locally clogged areas (Figure 11, top) within the pore network. This result underlines our previously made assumption of differential blocking of a small number of dominant flow paths during the injection. Accordingly, the resulting flow fields indicate a significant overall drop in flow velocity, especially close to the clogged regions (Figure 11, bottom). The highlighted areas within showcase highly frequent velocity changes on a smaller scale than before the clogging, which is most likely related to the forming of smaller pores in between the clogged particles.

Additionally, the total amount of deposited particle volume has been derived and analysed concerning the infiltration depth, i.e., in direction of flow (Figure 12). As for the laboratory experiment, we can observe a “deep” (relative to the size of the computational domain) infiltration of particles, i.e., half way into the digital sample. A main clogging region occurs about 1-1.5 mm deep into the sample. A second, less distinct area lies within 0.5 mm deep into the sample. Compared to Figure 10, we can link these regions directly to the blocked flow paths within our sample.

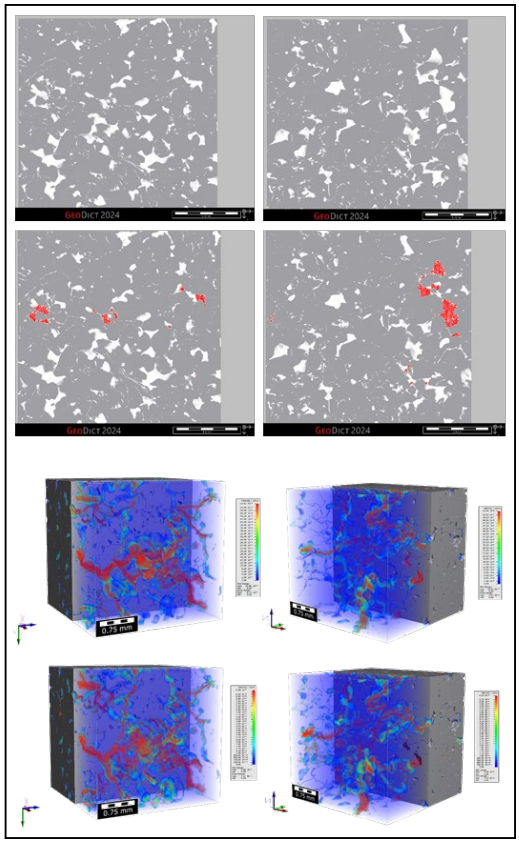

Fig. 11. 2D slices (left hand side) of selected regions before (top) and after (bottom) clogging simulation (red areas mark clogged pores) of the artificial sample. According velocity fields of the

flow simulations before (top) and after (bottom) clogging simulation. The flow velocity dropped by a factor of 7 in between and also shows high spatial variability in vicinity of the clogged regions.

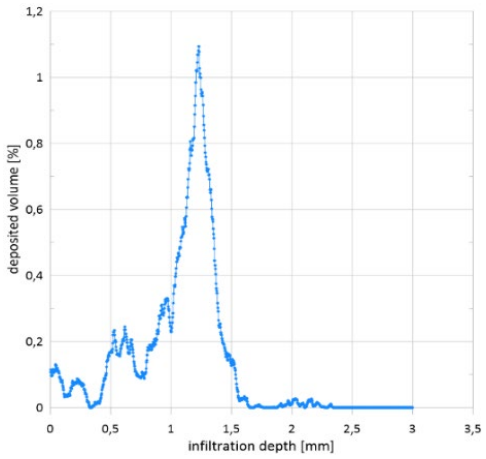

Fig. 12. Deposited particle volume versus infiltration depth into the artificial sample, derived by the clogging simulation. Main clogging occurs 1 – 1.5 mm deep into the sample.

Natural sample: Figure 13 displays the results of the MICP simulations before (Figure 13, blue line) and after (Figure 13, red line) the digital clogging. The dashed red line indicates changes in between. The overall reduction of volume fraction for pore throat diameters is more homogeneously distributed, compared to the artificial sample (see Figure 9). Nevertheless, again two "favorable" pore throat diameter ranges can be observed: from 20-30 µm and from 35 – 40 µm. These are almost the exact same spots as observed for the artificial sample. This reduction can be related to the clogging of flow paths within the domain. We do not observe an increase in smaller pore throats. In fact, the remaining throats in between these areas are remarkably constant and undisturbed, possibly indicating a very homogenous and "tight" packing of clogged particles.

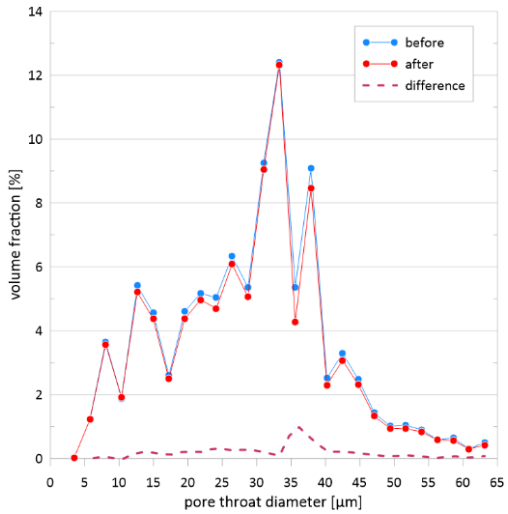

Fig. 13. Results of the MICP simulations for the natural sample, before (blue line) and after (red line) digital clogging. The dashed red line displays the difference of both curves.

Figure 14 displays the according distribution of permeability and porosity over time for the clogging simulation. Again, the overall change in porosity is not very remarkable, but at least constantly decreases during the simulation. In strong contrast to the artificial sample, permeability decrease over time is not very pronounced and follows a pretty constant, i.e., decreasing trend. This result facilitates our assumption that the clogging of particles obviously happened way more homogeneously, i.e., less locally clogged areas within the digital sample exist, leading to this result.

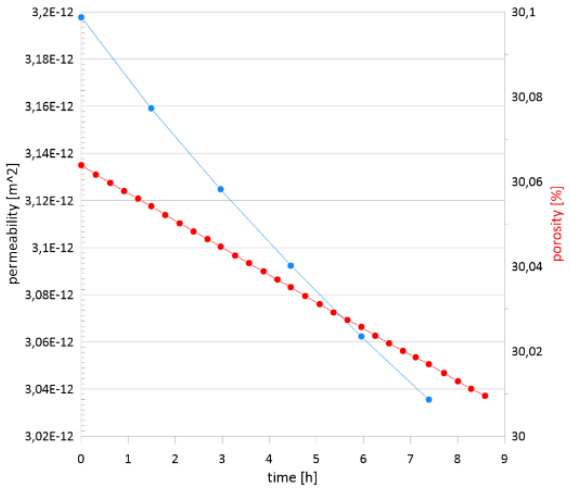

Fig. 14. Development of permeability for the natural sample during the digital clogging simulation (blue line). The red line displays the porosity change over time.

In fact, a close look into the digital sample before and after particle injection revealed very homogeneously distributed clogged areas (Figure 15, top) in close vicinity to the inflow region. This result again underlines our previously made assumption of a way more homogeneous pore blocking during the injection process. Accordingly, the resulting flow fields do not indicate any significant drop in flow velocity (Figure 15, bottom). We also do not see any highly frequent velocity changes on a smaller scale, which we linked to the forming of smaller pores in between the clogged particles for the artificial sample.

Additionally, the total amount of deposited particle volume has been derived and analysed concerning the infiltration depth, i.e., in direction of flow (Figure 16). As for the laboratory experiment, we can observe a "shallow" (relative to the size of the computational domain) infiltration of particles, i.e., less than 1/3 way into the digital sample. In contrast to the artificial sample, only

one main clogging region occurs, directly beginning at the inflow face and reaching about 0.5 mm deep into the sample. The rest of our injected particles is more or less linearly degrading distributed. This is conclusive to the findings as observed in Figure 15, displaying a more homogeneous distribution of clogged pores within the inflow area of our digital sample.

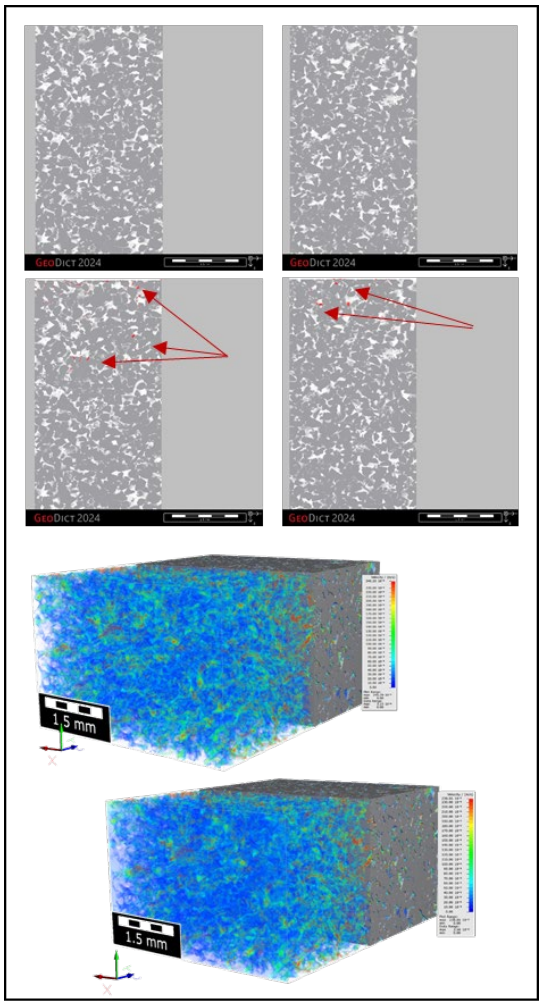

Fig. 15. 2D slices (left hand side) of selected regions before (top) and after (bottom) clogging simulation (red areas mark clogged pores) of the natural sample. According velocity fields of the flow simulations before (top) and after (bottom) clogging simulation. The flow velocity drop is barely noticeable, the infiltration more shallow and homogeneously distributed than for the artificial sample.

7 Conclusions

The mesoscale laboratory clogging investigation yielded results indicating that surface filtration at the sample inlet is an initial common response to clogging in both types of samples studied. The subsequent permeability behaviour is influenced by the complex structure of each specific sample group. However, the laboratory results clearly demonstrate that despite the artificial sample closely mimicking the porosity, permeability, and pore size distribution of the natural sample used, these two sample groups exhibit significant differences in behaviour.

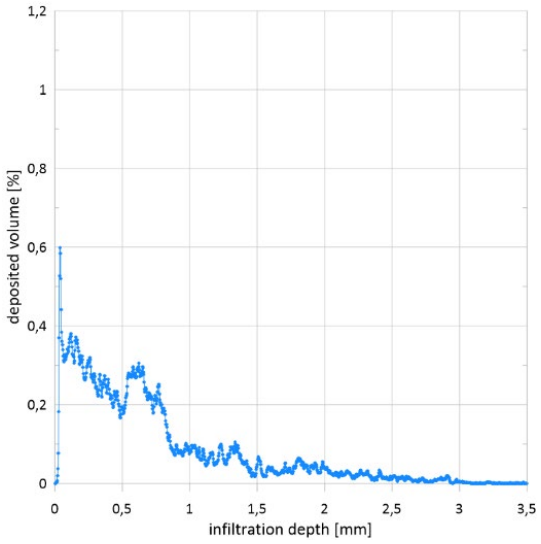

Fig. 16. Deposited particle volume versus infiltration depth into the natural sample, derived by the clogging simulation. Main clogging occurs within the very first 0.75 mm into the sample.

The experiments revealed distinct clogging mechanisms between artificial and natural samples. Artificial samples demonstrate the ability to adapt and reorganize their pore network, whereas natural samples exhibit a lack of recovery once clogging occurs. The control experiment and observed data suggest that while artificial samples may not exhibit long-term clogging in the laboratory, natural samples are more prone to experiencing a continuous decrease in permeability.

The image analysis and pore scale simulations widely confirmed the laboratory experiments. For the first time, systematic DRP clogging simulations have been carried out for this specific geothermal reservoir, utilizing the GeoDict toolbox. Furthermore, these simulations enabled us to achieve a significantly better understanding of spatial particle distributions, preferentially clogged flow paths and infiltration behaviour for our natural and artificial sample materials.

While artificial samples offer insights into initial clogging responses, natural samples provide a more accurate representation of the progressive clogging challenges encountered in actual geothermal operations. This understanding is crucial for predicting the long-term behaviour of geothermal reservoirs and designing effective interventions. The contrasting clogging observations underscore the necessity for tailored approaches in managing the injectivity of geothermal

reservoirs. For the future, we would like to extend this study by variations of clogging particle sizes, shapes and particle size distributions for both, laboratory experiments and digital rock physics simulations. Furthermore, the impact of formation compression, caused by too high injection pressures, as well as of anisotropy effects on the clogging processes will be investigated by DRP simulations.

The authors would like to acknowledge Dr. Stephan Kaufhold and Dr. Christian Ufer (both BGR, Hannover, Germany) for measuring and discussing the mineralogical composition of the investigated samples. Additionally, we extend our gratitude to Dr. Fedorné Szász Anita of Geochem Ltd. for analyzing the clogging particles used for the laboratory part of this research study. We thank our reviewers of the SCA´s Technical Board, Steffen Berg (Shell) and Jon Burger (Chevron), for reviewing and improving this manuscript.

References

1. A. Bálint, J. Szanyi, Centr. Europ. Geol., 58(1-2), 28-49 (2015).
2. A. Nádor, A. Kujbus, A. Tóth, European Geothermal Congress, Den Haag (2019).
3. J. Szanyi, T. Medgyes, B. Kóbor, E. Pál-Molnár, *Technologies of Injection into Sandstone Reservoirs: Best Practices, Case Studies, Szeged*, Magyarország GeoLitera (2015).
4. J. Szanyi, B. Kovács, Geothermics, Vol. 39 (2010).
5. Á. Markó, J., Mádl-Szőnyi, M. Brehme, Geothermics, Vol. 97 (2021).
6. M. Antics, *Simulation of Geothermal Reinjection Processes* (2017).
7. OGRE: the Online Hungarian Geothermal Information Platform, (2023) https://map.mbfsz.gov.hu/ogre_en.
8. J. Szanyi, B. Kovács, A. Hawkar, *Harnessing geothermal energy in Hungary. The Miocene Extensional Pannonian Superbasin,* Vol. 2: Geoenergy Exploration (The Geological Society of London, in press, 2024).
9. O. Sztanó, G. Tari, Tectonics and Eustasy Tectonophysics, Vol. 226, issues 1–4 (1993).
10. F. Horváth, G. Bada, P. Szafián, G. Tari, A. Ádám, S. Cloetingh, *Formation and Deformation of the Pannonian Basin: Constraints from Observational Data in European Lithosphere Dynamics* (Geological Society, London, Vol. 32, 2006).
11. W. Luo, A. Kottsova, P.J. Vardon, A.C. Dieudonné, M. Brehme, Renewable and Sustainable Energy Reviews, Vol. 185 (2023).
12. J.F. Bautista, A. Dahi Taleghani, Journal of Petroleum Science and Engineering, Vol. 164 (2018).
13. J. Haas, G. Hámor, Á. Jámbor, S. Kovács, A. Nagymarosy, *Geology of Hungary* (Springer-Verlag Berlin, 2013).
14. G. Juhász, Acta Geologica Hungarica, Vol. 34, No. 1–2 (1991).
15. J. Tóth, I. Almási, Geofluids, Vol. 1 (2001).
16. I. Almási, J. Szanyi, *Hydrogeology of the Pannonian Basin.* (The Groundwater Project, 2024).
17. F. Horváth, B. Musitz, A. Balázs, A. Végh, A. Uhrin, A. Nádor, B. Koroknai, N. Pap, T. Tóth, G. Wórum, Geothermics, Vol. 53 (2015).
18. D.H. Magyar, P. Müller, Palaeogeogr. Palaeclimatol. Paleoecol., Vol. 147 (1999).
19. L. Bereczki, L. Zilahi-Sebess, G. Markos, M. Kemény, E. Takács, *Database of the Hungarian Mining and Geological Survey* (2020).
20. Well Report, 2021: *Szentes K-712, Database of the Hungarian Mining and Geological Survey* (2021).
21. J. E. Cobos, E. G. Søgaard, *Geothermics*, Vol. 87 (2020).
22. Math2Market GmbH. (2024). GeoDict (SP1), https://www.math2market.com.
23. M. Halisch, M. Schmitt, C.P. Fernandes, *SCA Proceedings,* Snowmass, USA, SCA2016-093 (2016).
24. S. Linden, L. Cheng, A. Wiegmann, *Specialized methods for direct numerical simulations in porous media* (2018).
25. S. Linden, A. Wiegmann, H. Hagen, Graphical Models, Vol. 82 (2015).
26. X. Liu, A. Zhou, S. Shen, J. Li, Journal of Hydrology 612B, 128157 (2022).
27. V.P. Schulz, E.A. Wargo, E.C. Kumbur, Transport in Porous Media 107 (2014).
28. D. Silin, L. Tomutsa, S. Benson, T. Patzek, Transport in Porous Media 86 (2011).
29. J. Becker, V. Schulz, A. Wiegmann, Journal of Fuel Cell Science and Technology 5(2), 021006 (2008).
30. B. Ahrenholz; Advances in Water Resources 31 (2008).
31. D. Silin, T. Patzek, Physica A 371 (2006)
32. M. Hilpert, C. T. Miller, Advances in Water Resources 24 (2001).
33. R. D. Hazlett, Transport in Porous Media 20 (1995).
34. E. W. Washburn, Physical Review 17(3) (1921).
35. M. Thomeer, Journal of Petroleum Technology 12(3), SPE-1324-G (1960).